Research Article

Anti-Interference Heartbeat Measurement Based on a Miniaturized Doppler Radar Sensor

Lingtong Min [ID], Qinyi Lv [ID], Laisen Nie [ID], and Deyun Zhou [ID]

School of Electronics and Information, Northwestern Polytechnical University, Xi'an 710129, China

Correspondence should be addressed to Laisen Nie; nielaisen@nwpu.edu.cn

It is a hot topic to utilize the Doppler radar sensor in noncontact biosignal monitoring nowadays. Unfortunately, most detections are easily affected by interference or strong noise. Even slight body movements can cause serious demodulation distortion. In this paper, we proposed a novel algorithm to solve the sudden and unexpected interference. Firstly, the one-dimensional signal detected by the sensor is divided into segments to form a two-dimensional data matrix. In both the intrasegment and intersegment domains of the data matrix, a robust algorithm is employed to suppress unwanted interference, which significantly improves the robustness of demodulation. Experiments show the effectiveness of the proposed algorithm, based on which weak heartbeat signal hidden in the interference can be well extracted.

1. Introduction

The miniaturized continuous-wave Doppler radar sensors (DRS) have been extensively studied due to its crucial potential in human healthcare and monitoring applications [1, 2]. Admirable progress in past decades has been made to overcome challenges in small-scale motion monitoring. To solve the null point problems in small-angle approximation, quadrature demodulation was introduced [3]. Using arctangent demodulation to recover the accurate phase information was then reported [4]. The Doppler radar systems both based on instruments [5] and integrated on a single CMOS chip [6] have also been come up with to detect respiration and heartbeat. Some demodulation algorithms were also discussed [7–9]. DRS can also be used to detect other motions, such as animal biosignals [10], mechanical vibration measurement [11], gesture recognition [12], and rotation of wind turbine blades [13]. Nowadays, the basic approach of continuous-wave Doppler radar sensor is the demodulation of frequency shift in reflecting waves from the moving target. Since the phase demodulation method is a linear method and can achieve great accuracy, it has become the most popular and advanced demodulation approach [14].

The Doppler radar sensor is easily affected by interferences like random body movements (RBM). Firstly, random body movements occur naturally as far as the human body stands or sitting. When there exists body movement, especially in the strong case, large body movement will conceal the small biosignal and likely result in signal clipping in conventional DRS [9]. Multiple contributions have been done to deal with body movement problems [15–20]. In [15], two antennas are placed to detect from the front and the back of a human body simultaneously. In this way, biosignal can be enhanced because it exists from all sides; while body movement is cancelled by multiplying the signal detected from both sides. Also, circuit saturation is likely to happen in the presence of large body movement [16]. As for injection locking radars array in [17, 18], users have to either sweep the radar's carrier frequency or adjust the subject's position. The hybrid sensing system with both radar and camera is employed in [19]. This system shows good potential to cancel body movement but is still complex in both hardware and signal processing. All of the work presents complicated hardware architecture with high costs, and the detection is limited in the study of relatively small RBM.

What is more, SISO (single-in and single-out) Doppler radar architecture is only limited in one target detection.

In the scene of biosignal detection, if there exist other moving objects like pedestrian or part of moving limbs, mass distortion can be seen in the result. The system with multiple receiving channels can distinguish the multiple targets by the blind separation algorithm [20]. Radar with more complex waveforms can also detect multiple people [21]. But these architectures will also increase system cost and complexity.

In fact, the biosignal includes both heartbeat signal and respiration signal. But the respiration signal is always much stronger and more flat than the heartbeat signal, which makes heartbeat signal detection more difficult. As a consequence, more attention is paid to heartbeat signal detection. In our paper, we mainly focus on heartbeat signal reconstruction by radar.

In this paper, we propose a novel Doppler radar-based adaptive anti-interference algorithm to recover the heartbeat signal. The entire one-dimensional movement can be decomposed into several segments to form a new two-dimensional data matrix for further processing. Every segment in the intrasegment domain and adjacent segments in the intersegment domain are evaluated, respectively, by a well-designed criterion, including changes in signal strength and signal-to-noise ratio (SNR). A miniaturized radar operating at 24 GHz is employed to verify the effectiveness of our method.

The rest of this paper is organized as follows. In Section 2, the theory of Doppler radar is briefly introduced. Then we propose the anti-interference algorithm. To illustrate the effectiveness of the proposed approach, a series of noncontact measurements are performed in Section 3, and the obtained results are presented. Finally, a conclusion is drawn in Section 4.

2. Materials and Methods

2.1. Problem Description. A classical Doppler radar sensor is shown in Figure 1. The basic principle of DRS is the reflection of continuous wave modulated by a moving target, such as the human chest. As for a target at a distance d_0 with time-varying motion given by $x(t)$, the received signal is quadrature demodulated, and I/Q channels of the baseband signals are

$$I(t) = A_I(t) \cos \left[\theta_0 + \frac{4\pi x(t)}{\lambda} + \varphi_0(t) \right] + \mathrm{DC}_I(t), \quad (1)$$

$$Q(t) = A_Q(t) \sin \left[\theta_0 + \frac{4\pi x(t)}{\lambda} + \varphi_0(t) \right] + \mathrm{DC}_Q(t), \quad (2)$$

where $\mathrm{DC}_I(t), \mathrm{DC}_Q(t)$ denote the direct current offsets. $A_I(t), A_Q(t)$ denote the alternate current amplitudes, both of the output I/Q signals, respectively. $\varphi_0(t)$ denotes the residual phase noise of the receiver. θ_0 represents the phase shift accumulated due to the initial distance and transceiver system. From Equations (1) and (2), the motion $x(t)$ can be
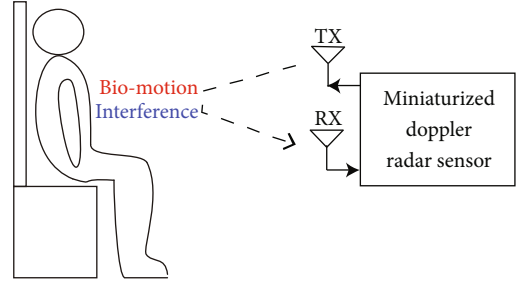

FIGURE 1: A classical radar system for biosignal detection including antennas, RF circuits to transmit and receive signals, and a signal processing unit. Interference is inventible during the detection.

mathematically expressed as

$$x(t) = \frac{\lambda}{4\pi} \left\{ \arctan \frac{[Q(t) - \mathrm{DC}_Q(t)]/A_Q(t)}{[I(t) - \mathrm{DC}_I(t)]/A_I(t)} - \theta_0 - \varphi_0(t) \right\}. \quad (3)$$

From Equation (1), we can conclude that the principal causes of nonlinearity in demodulation are the unknown DC offsets and the imbalance between $A_I(t)$ and $A_Q(t)$. The imbalance is mainly due to hardware architecture, namely the receiver, which can be mostly overcome by advanced digital downconversion [9]. Thus, in this paper, the imbalance is solved, and the amplitude of each channel is the same. $\mathrm{DC}_I(t)$ and $\mathrm{DC}_Q(t)$ are originally produced by the reflection of background. It is time-varying because the offset could be disturbed by multiple factors, such as limb waving and temperature drift of circuits. It is worth noting that the change of DC offset is usually slow. Given the facts above, the DC offset during the small piece of time, such as 1 or 2 seconds, can be treated as constant. In the following experiment part, 80 sampling points are chosen as the piece length, which is 0.9 second because the sampling rate is 90 Hz.

From another perspective to eliminate trigonometric functions, Equations (1) and (2) are rewritten as

$$\left(\frac{I(t) - \mathrm{DC}_I(t)}{A_I(t)} \right)^2 + \left(\frac{Q(t) - \mathrm{DC}_Q(t)}{A_Q(t)} \right)^2 = 1. \quad (4)$$

The I/Q signal is obviously forming ellipse, shown in Equation (2). Based on the facts and discussion above, the slow-varying DC offset is assumed as constant ($\mathrm{DC}_I[j]$ and $\mathrm{DC}_Q[j]$), where the index j represents the jth segment of the whole demodulation. Meanwhile, in the jth short time segment, the imbalance of quadrature signals can be overcome by the digital downconversion receiver [9]. The amplitude then also has be treated as constant in the jth segment, which is $A_I(t) = A_Q(t) = A[j]$. Consequently, the ellipse in Equation (4) is simplified into a circle:

$$(I(t) - \mathrm{DC}_I[j])^2 + (Q(t) - \mathrm{DC}_Q[j])^2 = A^2[j]. \quad (5)$$

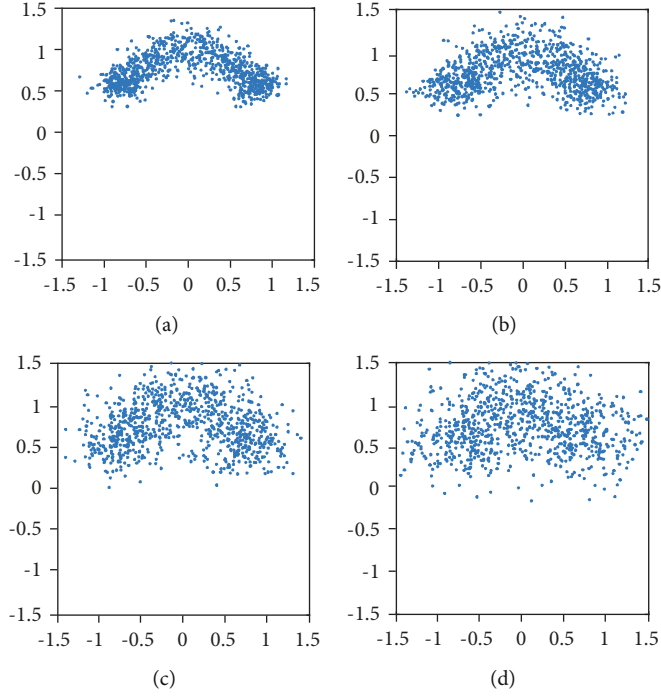It is seen that after eliminating the imbalance between

Figure 2: The constellations for simulated signal with different SNR: (a) SNR = 13 dB, (b) SNR = 10 dB, (c) SNR = 7 dB, and (d) SNR = 5 dB.

$I(t)$ and $Q(t)$ by digital-IF architecture, the ellipse turns into a circle, where the balanced amplitude is the radius $A[j]$, and the $(DC_I[j], DC_Q[j])$ is the center. In this ideal condition, as long as the circle center can be obtained from $I(t)$ and $Q(t)$, the motion $x(t)$ can be mathematically recovered.

The whole detection has been divided into m segments, and in each segment, the continuous-time variables are sampled into discrete series symbolled by index i. Equation (5) was then changed into

$$(I[i][j] - DC_I[j])^2 + (Q[i][j] - DC_Q[j])^2 = A^2[j]. \quad (6)$$

The whole detection sampling data array, containing m times n points and in one dimension, now is rearranged into 2-dimensional m times n matrix for further process. In the first dimension, i represents the sample point index in each segment, ranging from 1 to n. j represents the segment index, ranging from 1 to m.

In traditional pulse radar signal processing, the signal data matrix can be processed from the fast-time dimension and slow-time dimension, in which the range and speed are obtained, respectively. Inspired by this concept, we can analogically name the first dimension in the Doppler radar matrix as an intrasegment dimension, because the vector interval is the reciprocal of the sampling rate. The second dimension is called the intersegment dimension, and the interval is determined by segment length. The calculation based on the matrix is more effective and clearer.

In the following subsections, we will discuss how to arrange the matrix with the size of m times n. Then, in the intersegment domain, the optimization algorithm is developed to get a better result. In the intrasegment domain, the
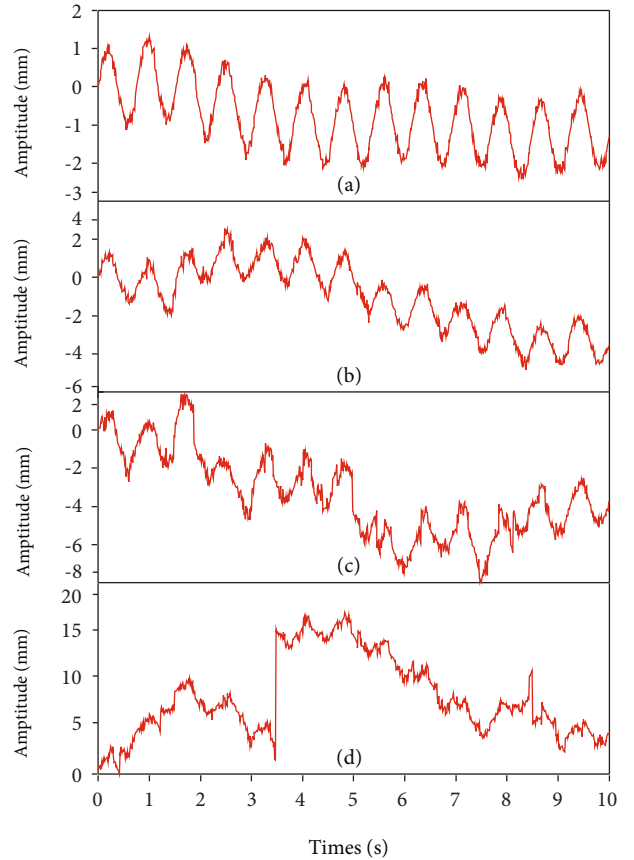

Figure 3: The demodulation result in time domain for simulated signal with different SNR: (a) SNR = 13 dB, (b) SNR = 10 dB, (c) SNR = 7 dB, and (d) SNR = 5 dB.
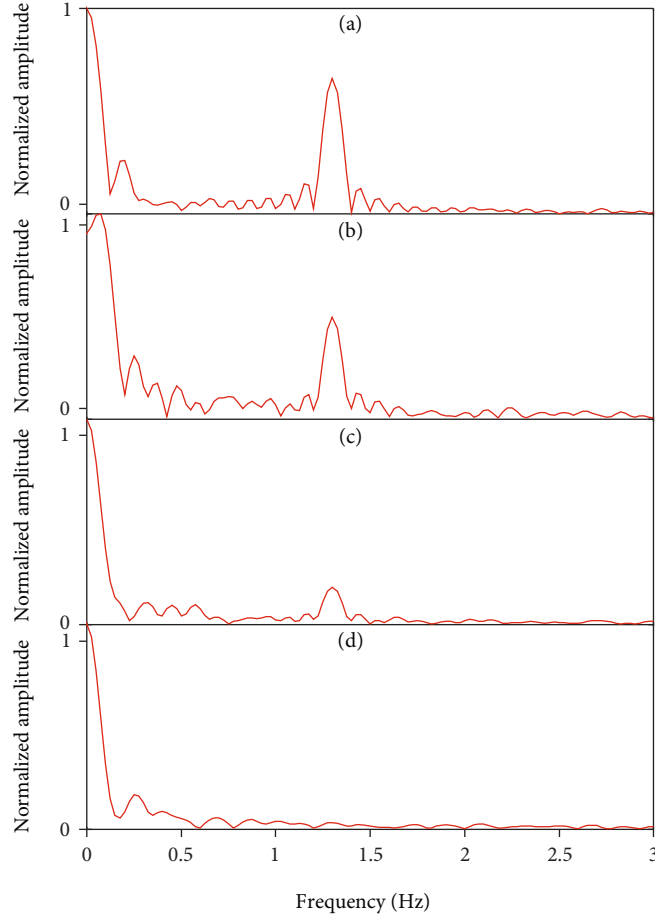
FIGURE 4: The demodulation result in frequency domain for simulated signal with different SNR: (a) SNR = 13 dB, (b) SNR = 10 dB, (c) SNR = 7 dB, and (d) SNR = 5 dB.

parameters produced by each segment in the intersegment domain are combined to access the fitness and adaptively filter out the interference.

2.2. The Demodulation and Optimization in Intrasegment Domain. In the segment j, the sampled I/Q signals can be expressed as a series $(I[1][j], Q[1][j]), (I[2][j], Q[2][j]), \cdots, (I[n][j], Q[n][j])$. The process of optimization can base on circle function. In this case, DC offset and radius are constant in each segment j. $(DC_I[j], DC_Q[j], A[j])$ are adjusted to form a circle and minimize deviation between the sampling series to the boundary of circle. According to (6), we define a loss function under a practical condition with noise

$$F(DC_I[j], DC_Q[j], A[j]) = \sum_{i=1}^{n} \left\{ (I[i][j] - DC_I[j])^2 \right.$$
$$\left. + (Q[i][j] - DC_Q[j])^2 - A[j]^2 \right\}.$$

(7)

The optimization algorithm minimizes the loss function as small as possible through an iterative process. When the loss function $F(DC_I[j], DC_Q[j], A[j])$ reaches its minimum, we take it as the optimal result. The parameters $(DC_I[j],$
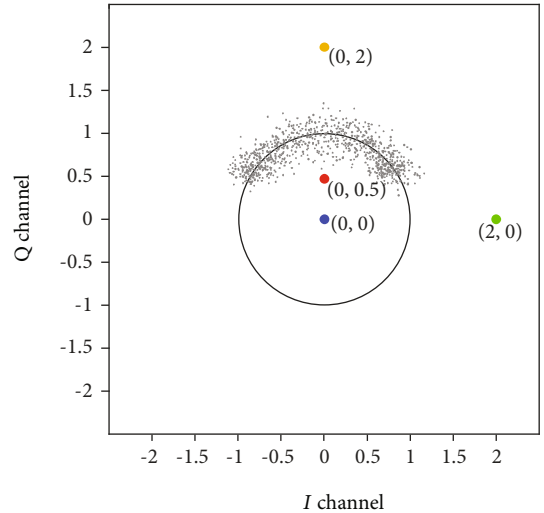

FIGURE 5: The constellation of simulated signal and four points for demodulation as DC offset: DC offset 1 (0, 0); DC offset 2 (0, 0.5); DC offset 3 (0, 2); and DC offset 4 (2, 0).
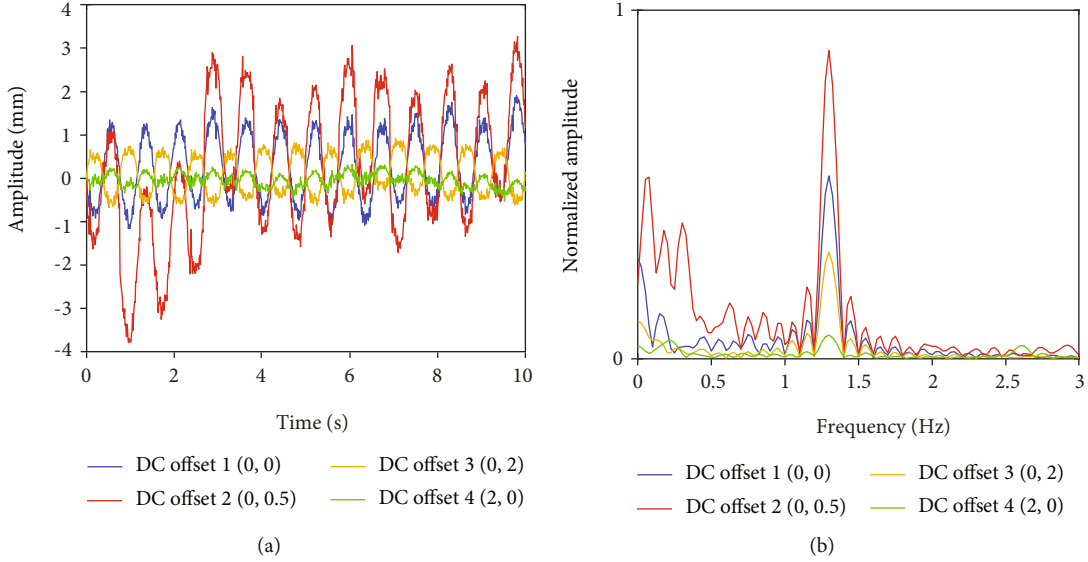
FIGURE 6: The demodulation result when four points are chosen for DC offset. (a) The result in time domain. (b) The result in frequency domain.

$DC_Q[j], A[j]$) will play an important role in evaluation to the degree of interference, which will be discussed in the next subsection.

After that, the extended DACM algorithm can retrieve the phase without phase wrapping problem, i.e.

$$\Phi(t) = \int_0^t \omega(t)dt = \int_0^t \frac{I(t)\dot{Q}(t) - \dot{I}(t)Q(t)}{I(t)^2 + Q(t)^2} dt. \quad (8)$$

Motion recovered by DACM will never encounter signal clipping caused by arctangent codomain. As a result, the instantaneous motion in each time slice can be linearly reconstructed.

2.3. DC Offset in the Demodulation.
The recovered motion $x(t)$ in each segment is just an ideal result. Concretely, the motion $x(t)$ is well reconstructed only when there exists one moving target with no strong interference. Next, we will analyze the influence of DC offset to demodulation in case of noises and interference.

The noise is reflected in both amplitude and phase. Correspondingly, in the following simulation, we add white noise to $A_I(t)/A_Q(t)$ and $\varphi_0(t)$ in Equations (1) and (2). The demodulation result with noise $xn(t)$ is expressed as

$$xn(t) = \frac{\lambda}{4\pi} \left\{ \arctan \frac{[Q(t) - DC_Q]/(A + \text{noise1})}{[I(t) - DC_I]/(A + \text{noise2})} - \text{noise3} \right\}, \quad (9)$$

where $A_I(t) = A + \text{noise1}$, $A_Q(t) = A + \text{noise2}$, and $\varphi_0(t) = \text{noise3}$. Here, θ_0 is ignored because we only care about the change of $xn(t)$, not the initial position.

The signal-to-noise ratio (SNR) in baseband is defined as $\text{SNR} = A^2/\text{noise\_power}$, where noise power is the square of noise variance. Phase noise has been discussed in reference
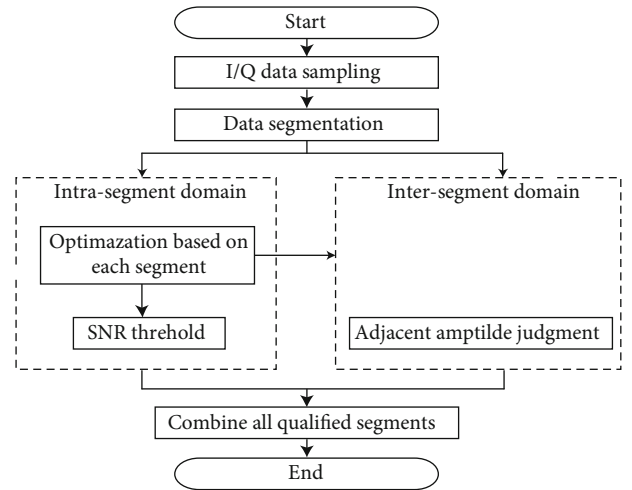

FIGURE 7: The flowchart of adaptive anti-interference algorithm.

[3], where the author concludes that although phase noise does affect the demodulation so much, it can still be neglected in most modern receivers.

To verify the influence of different SNR, we conducted a simulation. The heartbeat is assumed to 1.3 Hz, and four SNR are set as follows: 13 dB, 10 dB, 7 dB, and 5 dB. The DC offsets of each channel are 0. In Figure 2, four constellations can be observed. As the SNR degrading, the arc cannot be identified. But the demodulation still works until the SNR is lower than 7 dB, as shown in Figure 3 in time domain and Figure 4 in frequency domain. In practical detection for heartbeat signal signals, though the output power is limited, the SNR can be guaranteed to be large enough by designing proper antennas with high gain and constraining the measuring distance not to be too far.

In most cases, the phase is the ratio of arc to the radius. If the arc keeps constant, the radius is the inverse ration of
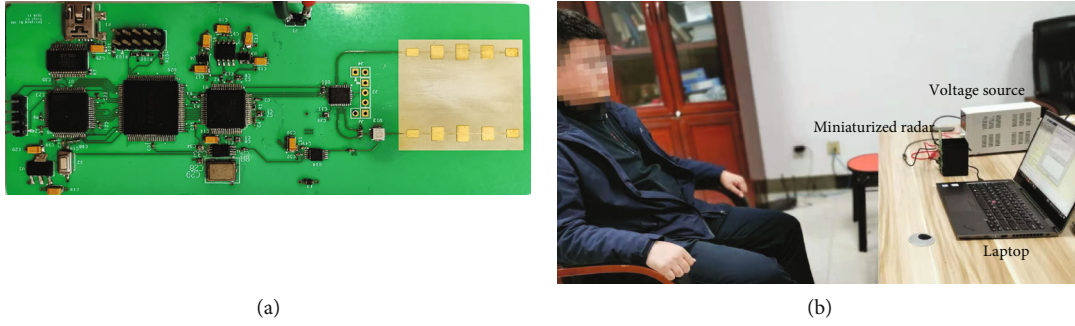
(a)

(b)

FIGURE 8: (a) The enlarged radar circuits viewed from front side and back side; (b) the setup of the experiment, including miniaturized radar, voltage source, laptop, and the subject under detection.
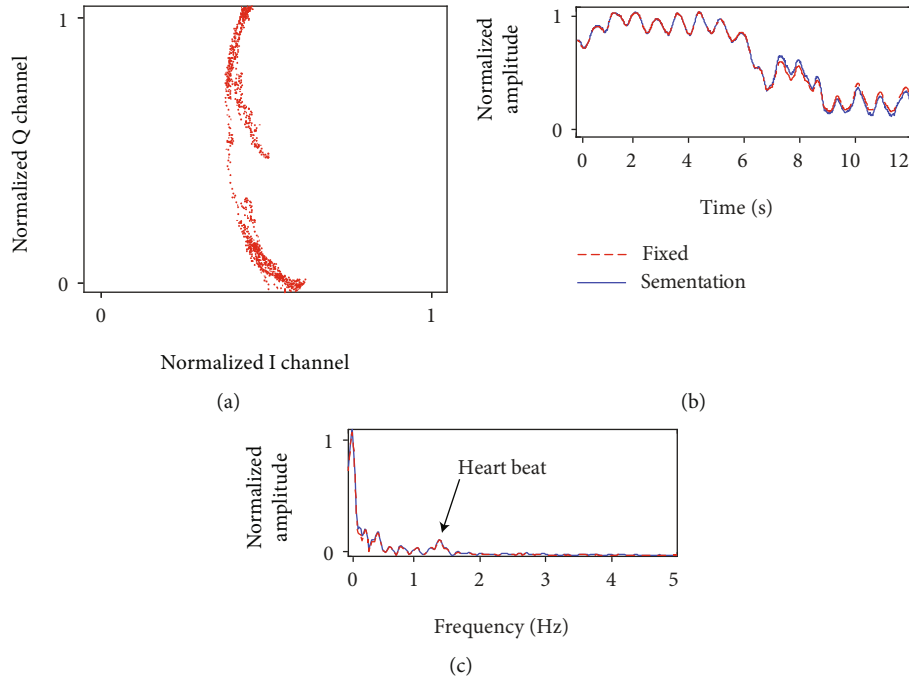

(a)

(b)

(c)

FIGURE 9: (a) *I/Q* constellation of biosignal when the subject tries to keep still. (b) Demodulation results in time domain by two methods: with segmentation or with fixed DC offset. (c) Demodulation results in frequency domain by two methods: with segmentation or with fixed DC offset.

movement. Following, the simulation is carried out to explore the impact of DC offset.

In the ideal case, if the DC offset is exactly located at the center of one circle, the demodulation of the Doppler signal can be effortlessly retrieved. However, in real cases, the center, which is decided by mathematical algorithms introduced in previous subsection, has the inevitable error. Small and trivial errors likely lead to significant demodulation distortion.

The second simulation is conducted to analyze this phenomenon. The frequency of heartbeat is set as 1.3 Hz like before, and the amplitude of heartbeat is 1 mm. The amplitude of each channel from the received signal is 1, and SNR is 13 dB. The original DC offset (center of the circle) is (0, 0) in ideal, which is named to DC offset 1. Then, we deliberately choose another three points deviated from the center (0, 0) as DC offsets in demodulation. DC offset 2

located at (0, 0.5) is closer to *I/Q* signal points; DC offset 3 is located at (0, 2), which is in the opposite direction of the real DC offset 1 (0, 0) to sampling points along the Q-channel-axis. DC offset 4 is (2, 0), in the I-channel-axis. All four DC offsets are marked in Figure 5, the constellation of sampling points.

In Figure 6(a), demodulation results in the time domain of four DC offset are shown. Recovered motion based on DC offset 1 (0, 0) is within expectation, and the amplitude of heartbeat is 1 mm. Because the DC offset 2 (0, 0.5) is closer to the sampling point, the demodulated amplitude is larger, near 2 mm. However, the tendency of whole motion is not stable because the noise affects the result more heavily as DC offset gets closer to sampling points. DC offset 3 (0, 2) is out of the circle formed by sampling data, but the heartbeat signal can still be observed from the demodulation result. The phase of the result is flipped 180 degrees. DC
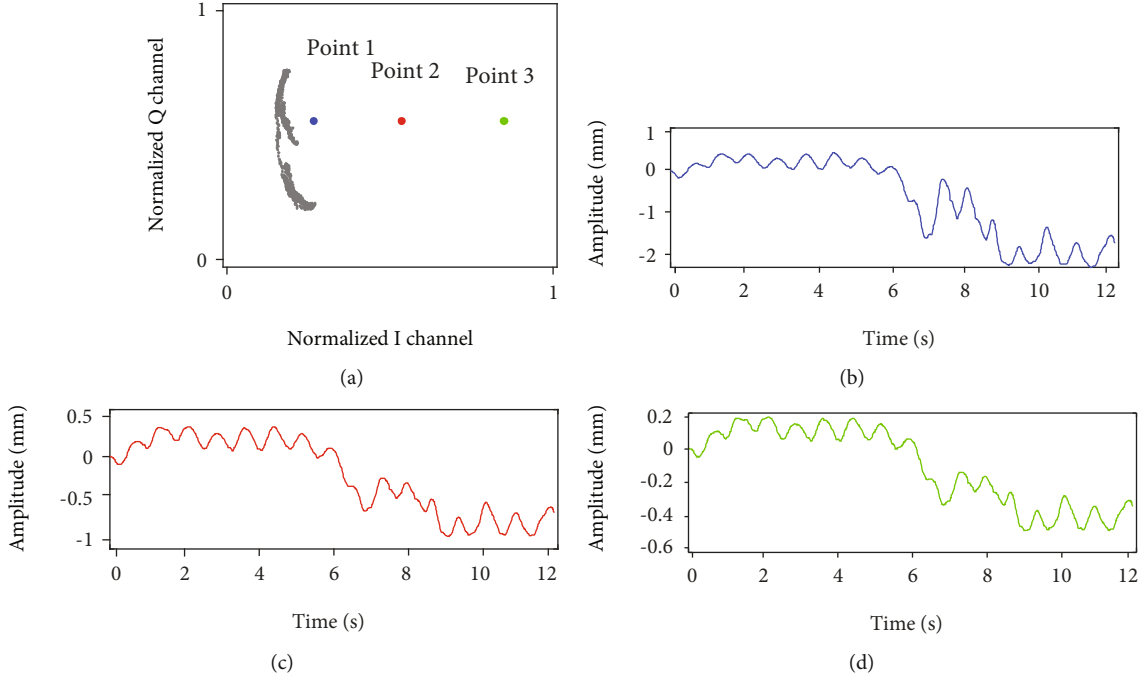
FIGURE 10: (a) *I/Q* constellation and the 3 points chosen as DC offset for demodulation. (b) Demodulation result when the DC offset is at point 1. (c) Demodulation result when the DC offset is at point 2. (d) Demodulation result when the DC offset is at point 3.

offset 4 is chosen along the I-channel-axis, and the corresponding result is much deteriorated.

In the frequency domain as shown in Figure 6(b), the heartbeat is visible under all the different DC offsets. The low-frequency noise is very obvious under DC offset 2, as we mentioned in time domain because of low SNR. Heartbeat signal is very weak under DC offset 4, and nonnegligible harmonic is located in 2.6 Hz.

In summary, the phase demodulation method is pretty robust for the DC offset with acceptable error. Nevertheless, the recover motion will be distorted when the noise is too strong or DC offset is chosen too far from the real center of sampling points. In other words, the validity of DC offset can be determined by SNR and signal intensity.

2.4. Adaptive Anti-Interference Algorithm.
As discussed above, now we find two parameters of prime importance: SNR and the signal intensity. In the practical measurement, we obtain only *I/Q* baseband signals. After the optimizations in Equation (6), DC offset $(DC_I[j], DC_Q[j])$ and the amplitude $A[j]$ can be reorganized to present the SNR and the signal intensity.

The noise of sampling points is expressed as a mean square error (MSE). Here the "mean" of sampling points is directly obtained by the optimized amplitude $A[j]$, not the average value of all distances between sampling data and DC offset.

$$MSE = \frac{1}{n}\sum_{i=1}^{n}\left(\sqrt{(I[i][j] - DC_I[j])^2 + (Q[i][j] - DC_Q[j])^2} - A[j]\right)^2.$$
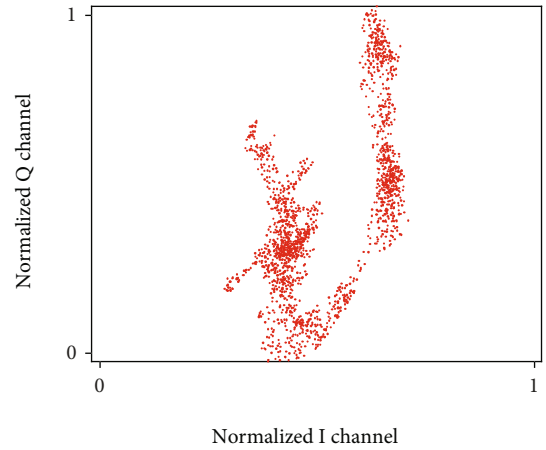
(10)

FIGURE 11: The constellation of *I/Q* signal when the subject under normal condition.

This MES can also be seen as the indicator of circle fitness. SNR is the ratio of signal to noise, which can be expressed as $A[j]^2/MSE^2$.

The signal intensity can be present by the amplitude in the baseband. As shown in Equation (6), the amplitude $A[j]$ in every segment is acquired by optimizing. In normal cases, adjacent $A[j]$ and $A[j-1]$ should not drastically change as the signal power is relatively stable. However, if interference and strong body movements occur, as discussed above, the $A[j]$ will be much bigger or smaller than the previous $A[j-1]$. As a result, we can construct a threshold between segments to determine whether there is strong interference.
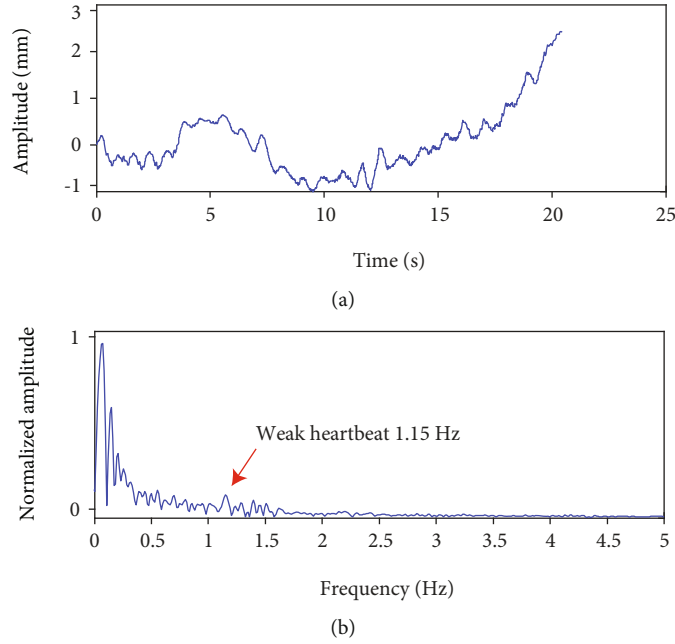
(a)

(b)

FIGURE 12: The demodulation result when using the fixed DC offset method. (a) In time domain. (b) In frequency domain.

Based on this idea, an adaptive anti-interference algorithm is come up with. This algorithm automatically judges whether there is too strong interference by identifying low SNR within the segment and dramatic change of $A[j]$ between segments. The SNR threshold is set to 7 dB as the first condition to decide whether this is a "bad segment." Another condition for "bad segment" is $A[j] > 3 A [j-1]$ or $A[j] > 3A A[j-1]$. If any of the two conditions is satisfied, the segment is determined as "bad segment" and discarded.

Figure 7 shows the flowchart of the adaptive anti-interference algorithm. When the detection starts, the radar samples the I/Q signal by quadrature downconversion. Then, the sampled data are divided into segments, and the data matrix is formed. In the intrasegment domain, every segment is optimized to obtain the best DC offset for demodulation. The process of optimization also gives us two parameters: radius directly and SNR indirectly after calculation. SNR in intrasegment domain is employed to judge whether each segment is qualified for demodulation or seriously interfered. And we also design a threshold based on the radius of adjacent segments in intersegment domain to decide whether this segment can be used for further process. To maintain the length of detection time window, we do not directly delete the "bad segments" with interference. Instead, we replace the "bad segment" with the qualified segment closest to it. At last, the segments that satisfied our standards in both intrasegment and intersegment domains are combined together. Because some "bad segments" are discarded, we also eliminate the discontinuous gap between the newly formed adjacent segments. Consequently, the splicing motion removes the interference and also avoids introducing new noise.

3. Results and Discussion

3.1. Hardware and Experiment Setup. Several experiments of different cases were conducted in order to validate the proposed approach. A 24 GHz miniaturized radar is employed, which is initially designed as digital-IF architecture to detect biosignal under body movement [19]. The system mainly bases on the monolithic millimeter-wave integrated circuit BGT24MTR11 produced by Infineon. The working principle of the circuit is as follows: First, the 24 GHz RF signal generated by the local oscillator (LO) is mixed with the low-IF signal generated by the waveform generator, and the signal is transmitted through the antenna; then, the receiving antenna receives the RF signal containing the motion information of the target to be measured. The signal is downmixed by the same LO to obtain a low-IF signal, and two orthogonal signals are generated during the quadrature downconversion process; in the next step, the low-IF analog signal is sampled by a 12-bit analog-digital conversion chip to obtain a quadrature digital signal; finally, the digital signal passes through the CPLD and the microprogrammed control unit (MCU) to reduce the data transmission rate to the computer for further processing; here, the MCU is also configured to control the main integrated circuit chips. The entire system is provided by a single crystal oscillator to provide the reference signal source, which ensuring the synchronization of the system and the coherence of the receiving and sending signals. The whole size of the printed circuit board (PCB) with four layers is about 14 cm × 5 cm, as shown in Figure 8(a). The transmitting power is set to 6 dBm, and the gain of the series-fed antenna is around 12 dBi. The sampling rate of analog-to-digital converter is 90 Hz.
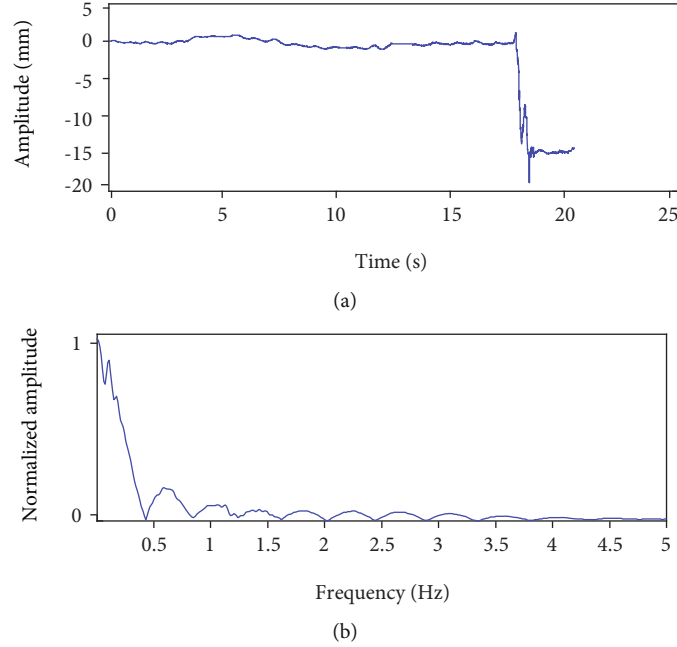
(a)

(b)

FIGURE 13: The demodulation result when using the multiple segments with different DC offset method. (a) In time domain. (b) In frequency domain.

The setup of experiments is shown in Figure 8(b). The 24 GHz miniaturized radar is placed vertically so that the antenna can transmit microwave signal to the subject. The voltage source is used to drive the circuits. The laptop receives the baseband I/Q signals through the USB port, and then, the data are processed in computer software.

In the biosignal measurement, the distance from the subject to antenna is about 50 cm. A 32-year-old male with 180 cm height is under detection. As discussed in Section 1, the subject always holds his breath to avoid respiration signal, and we only focus on heartbeat signal and interference.

3.2. Measurement on Different DC Offset. Before the measurement for more generalized cases with nonnegligible noise and interference, our first experiment is conducted when the subject tries his best to hold still. As shown in Figure 9(a), part of a circle formed by the I/Q series is clearly observed in the constellation. The fixed DC offset method and segmentation method with multiple DC offsets are, respectively, used to demodulate the motion from the phase. The recover motions in time domain and frequency domain are shown in Figures 9(b) and 9(c). Because, in this experiment, the noise and interference are very weak, no segment is judged as "bad segment" to be discarded, and there is no significant difference between the two methods.

Based on the same data, we also analyze the demodulation result with different DC offsets. In constellation shown in Figure 10(a), three DC offsets are chosen for motion recover: point 1, point 2, and point 3. Point 2 is close to the normal DC offset acquired by optimization. Point 1 is the DC offset very near to the I/Q signal arc, and point 3 is far from signal sampling points adversely. The modulation results in time domain are shown in Figures 10(b)–10(d).

TABLE 1: Main parameters of each segment in the experiment of heartbeat detection with interference.

Segment index j	DCI[j],	DCQ[j],	$A[j]$	SNR[j]
1	608526	-474756	8215	34
2	613464	-474613	3370	27
3	610951	-474800	5985	33
4	613463	-474421	3474	27
5	611635	-473168	5223	30
6	609639	-473656	7124	34
7	613312	-473079	3486	28
8	612722	-474169	4120	31
9	613108	-474565	3627	29
10	613371	-474731	3408	28
11	614357	-474357	3394	23
12	613495	-474406	3303	18
13	612278	-476394	2662	21
14	612952	-474742	2070	20
15	368166	-478876	246712	59
16	613134	-475000	2189	16
17	614693	-473513	2539	23
18	613542	-474391	2191	28
19	613582	-474346	2110	20
20	613061	-474980	2056	23
21	615021	-475248	190	3
22	613700	-473420	1904	18

All the results show the heartbeat signal obviously and are very similar in tendency. However, the amplitude of each recovered motion remains highly divergent. This corresponds well with the theoretical analysis. So, it is pretty
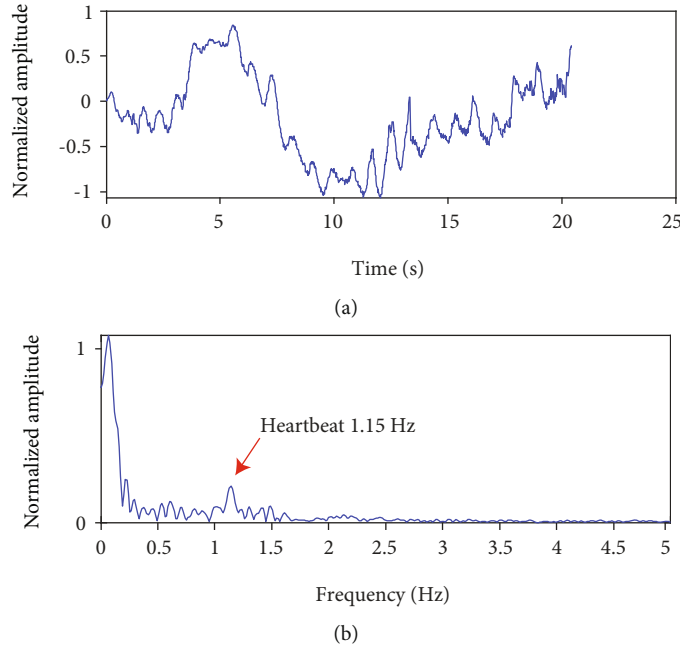
(a)

(b)

FIGURE 14: The demodulation result when using adaptive anti-interference algorithm. (a) In time domain. (b) In frequency domain.

robust for DC offset optimization to recover the frequency or time domain shape of the heartbeat. What really matters is the case with great interference and strong noise, and in the next subsection, we will solve this problem by the proposed adaptive anti-interference algorithm to filter the "bad segment" and reorganize the sampling series to recover heartbeat signal.

3.3. The Experiment of Heartbeat Detection with Interference. In this subsection, we conduct an experiment under normal conditions, in which there may be interference and strong noise. The subject tries to keep normally sitting, but uncontrolled random body movement (RBM) is inevitable.

The constellation shown in Figure 11 is much noisier than that in Section 3.2. Part of circles is still pretty evident, but not limited to only one circle center. Firstly, we still use the fixed DC offset. The demodulation result is shown in Figure 12. In time domain, the heartbeat signal can be seen, but the body movement is relatively strong, which is about 3.5 cm. In the frequency domain, the heartbeat signal is weak but still exists above noise floor at 1.15 Hz.

In Figure 13, the multiple segments with different DC offsets are used to recover the whole movement. It is obvious that the signal deformed seriously from 17 to 18 seconds. The cause is that the segment at that time encounters strong body movements, and the segment with fewer sampling points is interfered easily. In frequency domain, the heartbeat is totally concealed by the strong interference.

In Table 1, the corresponding parameters $DC_I[j], DC_Q[j], A[j]$ and SNR $[j]$ for each segment j are listed. As stated above, each segment contains 80 sampling point, that is about 0.9 second with 90 Hz sampling rate. It is obvious to notice that segment 15 and segment 21 are abnormal no matter from the perspective of $A[j]$ or SNR$[j]$. The segment

15 and 21 corresponds well with the sudden change occurs in Figure 13(a).

After applying our adaptive anti-interference algorithm, we can filter the "bad segment" which is with low SNR or deviated from the adjacent segment seriously in amplitude. The result is shown in Figure 14. In time domain, the heartbeat is obvious at 1.15 Hz, and the body movement in the whole detection is decreased to about 1.5 cm from 3.5 cm obtained by the demodulation algorithm with fixed DC offset. In frequency domain, the heartbeat signal has much better SNR in Figure 14(a) compared to the result in Figure 12(a). So, a more robust measurement of heartbeat with interference can be implemented.

From all the experiments, we can conclude that by using the proposed adaptive anti-interference algorithm, we can filter out the strong interference in normal detection for heartbeat signals. Better demodulation results can be obtained compared to the traditional method.

This method is effective for sudden and short-term interference as demonstrated above. However, if the interference lasts for a long time such as 30 seconds, this method is likely to fail. Due to the iterative process of the DC offset as shown in Equation (7), the algorithm takes a little longer. This also needs to be overcome to realize real-time measurement.

4. Conclusions

In conclusion, we come up with a novel anti-interference algorithm in the detection of biosignal, applied to scenarios with motion with strong interference or noise, just like the case of random body movement. Specifically, the signal-to-noise ratio threshold in intrasegment domain and signal strength comparison of adjacent segments in the intersegment domain are used as a criterion for determining

whether there is strong interference. The unqualified segments will be automatically replaced by the qualified ones, and all the segments are reorganized together at last. This algorithm can improve the performance of heartbeat detection in both the time domain and frequency domain. After theoretical analyses, simulations and experiments are conducted to validate the proposed method. This novel method makes the application of the Doppler radar in the field of biosignal detection more universal and promising in daily activities.

Data Availability

The data used to support the findings of this study have not been made available because of the potential privacy.

Conflicts of Interest

The authors declare that there is no conflict of interest regarding the publication of this paper.

Authors' Contributions

Lingtong Min and Qinyi Lv are co-first authors.

Acknowledgments

References

[1] C. Li, V. M. Lubecke, O. Boric-Lubecke, and J. Lin, "A review on recent advances in Doppler radar sensors for noncontact healthcare monitoring," *IEEE Transactions on Microwave Theory and Techniques*, vol. 61, no. 5, pp. 2046–2060, 2013.

[2] C. Li, Z. Peng, T. Y. Huang et al., "A review on recent progress of portable short-range noncontact microwave radar systems," *IEEE Transactions on Microwave Theory and Techniques*, vol. 65, no. 5, pp. 1692–1706, 2017.

[3] A. D. Droitcour, O. Boric-Lubecke, V. M. Lubecke, J. Lin, and G. T. A. Kovac, "Range correlation and I/Q performance benefits in single-chip silicon Doppler radars for noncontact cardiopulmonary monitoring," *IEEE Transactions on Microwave Theory and Techniques*, vol. 52, no. 3, pp. 838–848, 2004.

[4] B. K. Park, O. Boric-Lubecke, and V. M. Lubecke, "Arctangent demodulation with DC offset compensation in quadrature Doppler radar receiver systems," *IEEE Transactions on Microwave Theory and Techniques*, vol. 55, no. 5, pp. 1073–1079, 2007.

[5] J. Wang, X. Wang, J. Huangfu, C. Li, and L. Ran, "Noncontact distance and amplitude-independent vibration measurement based on an extended DACM algorithm," *IEEE Transactions on Instrumentation and Measurement*, vol. 63, no. 1, pp. 145–153, 2014.

[6] C. Li, X. Yu, C. Lee, L. Ran, and J. Lin, "High-sensitivity software-configurable 5.8-GHz radar sensor receiver chip in 0.13-μm CMOS for noncontact vital sign detection," *IEEE Transactions on Microwave Theory and Techniques*, vol. 52, no. 5, pp. 1410–1419, 2010.

[7] Q. Lv, D. Ye, S. Qiao et al., "High dynamic-range motion imaging based on linearized Doppler radar sensor," *IEEE Transactions on Microwave Theory and Techniques*, vol. 62, no. 9, pp. 1837–1846, 2014.

[8] T. Fan, C. Ma, Z. Gu et al., "Wireless hand gesture recognition based on continuous-wave Doppler radar sensors," *IEEE Transactions on Microwave Theory and Techniques*, vol. 64, no. 11, pp. 4012–4020, 2016.

[9] J. Wang, X. Wang, Z. Zhu, J. Huangfu, C. Li, and L. Ran, "1-D microwave imaging of human cardiac motion: an ab-initio investigation," *IEEE Transactions on Microwave Theory and Techniques*, vol. 61, no. 5, pp. 2101–2107, 2013.

[10] N. Hafner, J. C. Drazen, and V. M. Lubecke, "Fish heart rate monitoring by body-contact Doppler radar," *IEEE Sensors Journal*, vol. 13, no. 1, pp. 408–414, 2012.

[11] B. Spencer Jr., S. Cho, and S.-H. Sim, "Wireless monitoring of civil infrastructure comes of age," *Structure*, vol. 13, pp. 12–16, 2011.

[12] Y. Zhang, S. Dong, C. Zhu, M. Balle, B. Zhang, and L. Ran, "Hand Gesture Recognition for Smart Devices by Classifying Deterministic Doppler Signals," *IEEE Transactions on Microwave Theory and Techniques*, vol. 69, no. 1, pp. 365–377, 2021.

[13] A. Naqvi, S.-T. Yang, and H. Ling, "Investigation of Doppler features from wind turbine scattering," *IEEE Antennas and Wireless Propagation Letters*, vol. 9, pp. 485–488, 2010.

[14] S. Dong, Y. Zhang, C. Ma et al., "Doppler cardiogram: a remote detection of human heart activities," *IEEE Transactions on Microwave Theory and Techniques*, vol. 68, no. 3, pp. 1132–1141, 2020.

[15] C. Li and J. Lin, "Random body movement cancellation in Doppler radar vital sign detection," *IEEE Transactions on Microwave Theory and Techniques*, vol. 56, no. 12, pp. 3143–3152, 2008.

[16] F. K. Wang, T. S. Horng, K. C. Peng, J. K. Jau, J. Y. Li, and C. C. Chen, "Single-antenna Doppler radars using self and mutual injection locking for vital sign detection with random body movement cancellation," *IEEE Transactions on Microwave Theory and Techniques*, vol. 59, no. 12, pp. 3577–3587, 2011.

[17] M.-C. Tang, C.-Y. Kuo, D.-C. Wun, F.-K. Wang, and T.-S. Horng, "A self- and mutually injection-locked radar system for monitoring vital signs in real time with random body movement cancellation," *IEEE Transactions on Microwave Theory and Techniques*, vol. 64, no. 12, pp. 4812–4822, 2016.

[18] C. Gu, G. Wang, Y. Li, T. Inoue, and C. Li, "A hybrid radar-camera sensing system with phase compensation for random body movement cancellation in Doppler vital sign detection," *IEEE Transactions on Microwave Theory and Techniques*, vol. 61, no. 12, pp. 4678–4688, 2013.

[19] Q. Lv, L. Chen, K. An et al., "Doppler vital signs detection in the presence of large-scale random body movements," *IEEE Transactions on Microwave Theory and Techniques*, vol. 66, no. 9, pp. 4261–4270, 2018.

[20] Z. Gu, T. Fan, Q. Lv et al., "Remote blind motion separation using a single-tone SIMO Doppler radar sensor," *IEEE Transactions on Geoscience and Remote Sensing*, vol. 57, no. 1, pp. 462–472, 2019.

[21] M. Mercuri, I. R. Lorato, Y.-H. Liu, F. Wieringa, C. Van Hoof, and T. Torfs, "Vital-sign monitoring and spatial tracking of multiple people using a contactless radar-based sensor," *Nature Electronics*, vol. 2, no. 6, pp. 252–262, 2019.